PAPER • OPEN ACCESS

Post-mortem analysis of the erosion/deposition pattern on ITER-like actively cooled W-monoblock from the WEST divertor (Phase I)

To cite this article: P. Tsavalas *et al* 2026 *Nucl. Fusion* **66** 036046

OPEN ACCESS
IOP Publishing | International Atomic Energy Agency
Nuclear Fusion
Nucl. Fusion **66** (2026) 036046 (20pp)
https://doi.org/10.1088/1741-4326/ae3ab3

Post-mortem analysis of the erosion/deposition pattern on ITER-like actively cooled W-monoblock from the WEST divertor (Phase I)

P. Tsavalas[1,*], K. Mergia[1], M. Axiotis[2], A. Benmoumen[3], I. Bogdanovic Radovic[4], M. Diez[5], E. Fortuna-Zaleśna[6], A. Hakola[7], A. Lagoyannis[2], C. Martin[3], D. Papadakis[1], Z. Siketic[4], M. Spychalski[6] and WEST Team[a]

[1] Institute of Nuclear and Radiological Sciences and Technology, Energy and Safety, National Centre for Scientific Research 'Demokritos', 15310 Aghia Paraskevi, Athens, Greece
[2] Institute of Nuclear and Particle Physics, National Centre for Scientific Research 'Demokritos', 15310 Aghia Paraskevi, Athens, Greece
[3] Aix Marseille University, CNRS, PIIM, Marseille, France
[4] Ruđer Bošković Institute, Bijenička 54, 10000 Zagreb, Croatia
[5] CEA, IRFM, F-13108 Saint-Paul-Lez-Durance, France
[6] Faculty of Materials Science and Engineering, Warsaw University of Technology, Woloska 141, Warsaw 02-507, Poland
[7] VTT Technical Research Centre of Finland Ltd, Espoo, Finland

E-mail: ptsavalas@ipta.demokritos.gr

Received 16 July 2025, revised 19 December 2025
Accepted for publication 20 January 2026
Published 24 February 2026

Abstract

During Phase I of WEST operation, one of the lower divertor sectors, known as the test sector, was partially equipped with actively cooled ITER-like plasma-facing units (PFUs) made of 35 monoblocks (MBs). A visual inspection of the test sector after the C4 campaign revealed changes on the surface condition of several MBs located in the outer strike area. In this work, one of the MBs of interest, MB 28 from PFU#13, was extensively investigated focusing on fuel retention, material migration (erosion, transport, redeposition), and surface morphology. The plasma exposed surface of MB 28 exhibited four distinct zones along the toroidal direction. In the first zone, extending up to 4 mm from the leading edge (LE), the surface showed signs of erosion, with periodically spaced cracks oriented perpendicular to the LE. The second zone exhibited the highest material deposition (B, N, Fe and Cu) and fuel (D and He) retention, with the maximum deposit thickness reaching approximately 1.5 μm. In the third zone, the deposition gradually decreased and accumulated in linear areas. The fourth zone, near the trailing edge,

[a] See http://west.cea.fr/WESTteam.
[*] Author to whom any correspondence should be addressed.

was marked by the maximum hydrogen (*H*) and carbon (*C*) deposition. In this zone, linear deposition areas rich in O and B were detected, running parallel to the edge. A clear correlation was observed between the deposition of B, N, Fe and Cu and the retention of D and He.

Keywords: tungsten, actively cooled divertor, ion beam analysis, scanning electron microscopy, WEST tokamak, erosion, material deposition

(Some figures may appear in colour only in the online journal)

1. Introduction

Plasma–wall interaction (PWI) [1, 2], namely erosion, material migration, deposition, and fuel retention, is a critical issue for fusion devices as it determines the lifetime of plasma-facing components and strongly influences overall plasma stability [3]. Following the recent ITER re-baseline to a full-tungsten device, plasma–material interaction studies conducted on WEST have gained increased significance, as they directly address key challenges associated with tungsten plasma-facing components under long-pulse, high-heat-flux operation. Tungsten (W) has been selected for the plasma-facing components [4, 5] due to its high melting point, high thermal conductivity, thermal stress and shock resistance and high temperature strength [6], low erosion [7] and low fuel retention [8]. The interaction of the tungsten wall with the plasma has been investigated through numerical simulations [9] and experiments in several W-upgraded fusion devices, such as the ASDEX Upgrade [10], JET [11], WEST [12, 13] and KSTAR [14]. A comprehensive overview of the recent simulation and experimental results is presented in [15].

During Phase I of WEST operation (2016–2020), five experimental campaigns were carried out, identified as C1 to C5 [16]. The WEST lower divertor consisted of 12 independent toroidal sectors of 30° each composing 38 targets. A total of 10 of these sectors were equipped with inertially cooled (IC) graphite tiles coated with a Mo interlayer and a 12 μm top W layer. Part of one sector (Q2A) was fitted with marker tiles (CFC/Mo/W/Mo/W) while another one of the sectors, referred to as 'test sector' (identified as Q3B [17]), was partially equipped with actively cooled ITER-like plasma facing units (PFUs). Each PFU consisted of 35 non-beveled W monoblocks (MBs) bonded to a CuCrZr cooling tube [12].

Following Phase I, numerous studies investigated the interaction between the marker tiles and the plasma [18–21], while others [22, 23] examined the pre-damaged ITER-like PFUs. Additional research, using both modeling and experimental data, focused on the effects of heat loads [24–28], temperature [29, 30] and their correlation with cracks [31, 32], melting [33] and the emissivity [34–36] of the PFU.

The plasma exposure left its footprint on the test sector surface. The observed pattern allowed to identify the type of plasma–surface interactions occurring along the divertor targets: redeposition between MB 1–13, erosion between MB 14–17 and MB 23–29 and almost no interactions on the rest of the MBs [17]. In the [37], one sample from each region was analyzed using x-ray photoelectron spectroscopy.

Visual inspection of the test sector after the C4 campaign revealed significant changes on the surface condition of certain MBs [38]. In the present work we investigate one particular monoblock, MB 28, from the PFU located at position 13 in this sector. MB 28 was selected due to its distinctive features that make it particularly informative for understanding PWIs under ITER-relevant conditions: Firstly, MB 28 was located in the outer strike point (OSP) area, which experiences the highest heat and particle fluxes, and is therefore expected to undergo the most pronounced erosion and surface modifications. Secondly, this MB was exposed to the helium campaign during C4 [39, 40], providing a unique opportunity to investigate the effects of helium plasmas—including bubble formation, nano-structuring, and surface roughening—on tungsten surfaces in a real tokamak environment. Most notably MB 28 exhibited clear surface changes along its toroidal direction, characterized by variations in color and contrast. This change of color/contrast is mainly due to the fact that MB 28 PFU#13 was vertically misaligned, during C4, of about +0.3 mm with respect to upstream neighbor PFU#12 [38].

The primary objective of this study is to systematically investigate material deposition, fuel retention, and surface morphological changes on an actively cooled ITER-like MB using post-mortem analysis techniques, with a spatial resolution finer than that of previous studies [17]. By doing so, the results from MB 28 provide critical insight into the mechanisms of tungsten erosion, re-deposition, and defect formation under long-pulse plasma operation, supporting improved modeling and predictive capabilities for ITER and future fusion devices.

The manuscript is structured as follows: In section 2 the divertor configuration in WEST and the operating conditions are described, along with the experimental methods employed. Section 3 presents the experimental results, beginning with an overview of the MB 28 surface, followed by an analysis of surface morphology changes, and concluding with material deposition and fuel retention from ion beam analytical techniques. In section 4 the results in relation to the WEST tokamak operation during the C3 and C4 campaigns are discussed, and in section 5 a summary of the key findings is provided.

2. Experimental details

2.1. Divertor configuration and operating conditions

Figure 1(*a*) presents an overview of the interior of the WEST vacuum vessel during the C3 campaign, noting the various

parts of the first wall [16]. The configuration of the divertor test sector from the C3 and C4 are depicted in figures 1(*b*) and (*c*), respectively. In C3 campaign the PFU#20 and in C4 the PFU#7 were pre-damaged. Figure 1(*d*) depicts the normalized heat flux and the ripple effect on the sector Q3B. The schematic representation of the analyzed MB is shown in figure 1(*e*). It consists of a tungsten block bonded to a CuCrZr heat sink tube using a pure copper interlayer to reduce the thermo-mechanical stresses resulting from the thermal expansion mismatch of the bonded materials [12]. The tungsten block has a 1 mm chamfer at both leading and trailing edges (TEs). Apart from the plasma exposed surface of MB 28, a sample from the bottom surface (non-exposed) of the MB was cut to be used as reference. The reference sample was measured before and after electropolishing. The exposed and the reference samples were stored under vacuum until the experimental measurements.

The plasma exposed surface of tungsten MB 28 from the ITER-like PFU#13 that had been exposed to the C3 (deuterium plasma) and C4 (deuterium and helium plasma) experimental campaigns was investigated. During these campaigns, several boronization procedures were performed, depositing a thin boron layer on the surface of the W wall. This layer getters oxygen, reducing O impurities in the plasma and mitigating radiative losses, while also preventing W erosion. The main parameters of the two campaigns are presented in table 1.

It is noted that during Phase I, no thermocouples or fiber Bragg gratings were installed on the ITER-like PFUs. The temperature of the tungsten MBs during the operation could only be assessed from the images of the VHR IR (Very High Resolution Infra-Red) system. The VHR camera can only monitor a couple of MBs *in-situ* and the MB studied in this paper (MB 28, PFU#13) was not under surveillance during the campaign.

2.2. Experimental methods

2.2.1. Optical microscopy. The optical images and topography of odd and non-exposed MBs from MB 19 to MB 35 in the OSP region were obtained using the S neox confocal microscope from SENSOFAR equipped with a CCD camera (1360 $\times$ 1024 pixels). For the block imaging, 5 $\times$ 13 image stitching is used. The roughness (Sa values) of odd and non-exposed MBs from MB 19 to MB 35 in the OSP region were determined from 3 $\times$ 4 mm^2 images with spatial sampling of 645 nm. After image processing including levelling and applying a Gaussian filter with a 0.8 mm cutoff, the roughness values were determined to range from 0.62 to 0.45 μm for the center of the MBs. We estimated the roughness of the non-exposed MB 28 to be (0.50 $\pm$ 0.05) μm based on the average of these values, as unfortunately it was not measured directly.

2.2.2. Optical profilometry. The roughness of the exposed surface was determined using the Profilm3D® from the Filmetrics [41]. Fourteen areas, having a surface of 1.0 $\times$ 0.85 mm^2, were analyzed along the toroidal direction, with a 2 mm spacing between each area.

2.2.3. Scanning electron microscopy (SEM) with energy dispersive x-ray (EDX) spectroscopy, optical profilometry and focused ion beam (FIB) cross-sectioning SEM. SEM measurements were carried out using the ThermoFisher scientific Apreo 2 field emission gun scanning electron microscope (FE-SEM). Additionally, EDX spectroscopy and elemental mapping for the same areas were carried out employing an Oxford Instruments ULTIM-MAX Silicon Drift 65 mm^2 area detector and the Aztec Advanced Live Package software. For the elemental quantification a 5 keV electron beam was used. A Hitachi SU-8000 FE-SEM equipped with EDX spectrometer, Thermo Scientific, was combined with optical profilometry (Veeco NT9300) in order to determine how the deposit forms on the surface.

FIB cross-sectioning SEM (FIB/SEM Hitachi NB5000) was employed to investigate the internal structure of both the deposit and the features present on the MB.

2.2.4. Nuclear reaction analysis (NRA). The NRA measurements were carried out at the 5.5 MV Tandem Accelerator Laboratory of NCSR 'Demokritos', Athens, Greece employing a 1.6 MeV deuteron beam. The experimental setup is placed in a C. Evans & Assoc. scattering chamber which was under vacuum (10^{-7} mbar) during the measurement. The products were detected by a silicon surface-barrier detector placed at 170° with respect to the beam axis. A Kapton® foil was placed between the detector and the samples in order to absorb the backscattered deuteron so that the dead time and the pile-up decreased. The ^{12}C(d,p$_0$)^{13}C, ^{14}N(d,a$_1$)^{12}C and ^{16}O(d,p$_0$)^{17}C reaction peaks were simulated using the cross section from the SigmaCalc archive to obtain C, N, and O surface densities on the surface [42]. The boron quantification was determined from the ^{11}B(d,a$_0$)^{9}Be peak using the Kokkoris *et al* [43] cross section. The ^{11}B(d,p$_0$)^{12}B and ^{10}B(d,p$_{2,3,4,5}$)^{11}B were also simulated using Kokkoris *et al* [43, 44] cross sections, respectively. For the deuterium retention the D(d,p$_0$)T peak was simulated using the scaled W. Gruebler *et al* [45] cross sections. The cross sections were scaled employing a previous set of samples so that the amount of deuterium with the deuteron beam coincides with the results of the ^{3}He beam measurements [46]. The diameter of the circular beam spot was about 2 mm. Fourteen points along the toroidal direction were measured, with a 2 mm spacing between each beam spot.

2.2.5. Time of flight elastic recoil detection analysis (Tof-ERDA). The elemental composition in the first 150 nm of depth (in at%) was determined using Tof-ERDA. The Tof-ERDA measurements were performed at the 6 MV tandem van de Graaff accelerator at the Ruđer Bošković Institute in Croatia. 23 MeV ^{127}I^{8+} ions hit the sample at an angle of incidence of 20° to the sample surface. The Tof-ERDA spectrometer was positioned at an angle of 37.5° relative to the

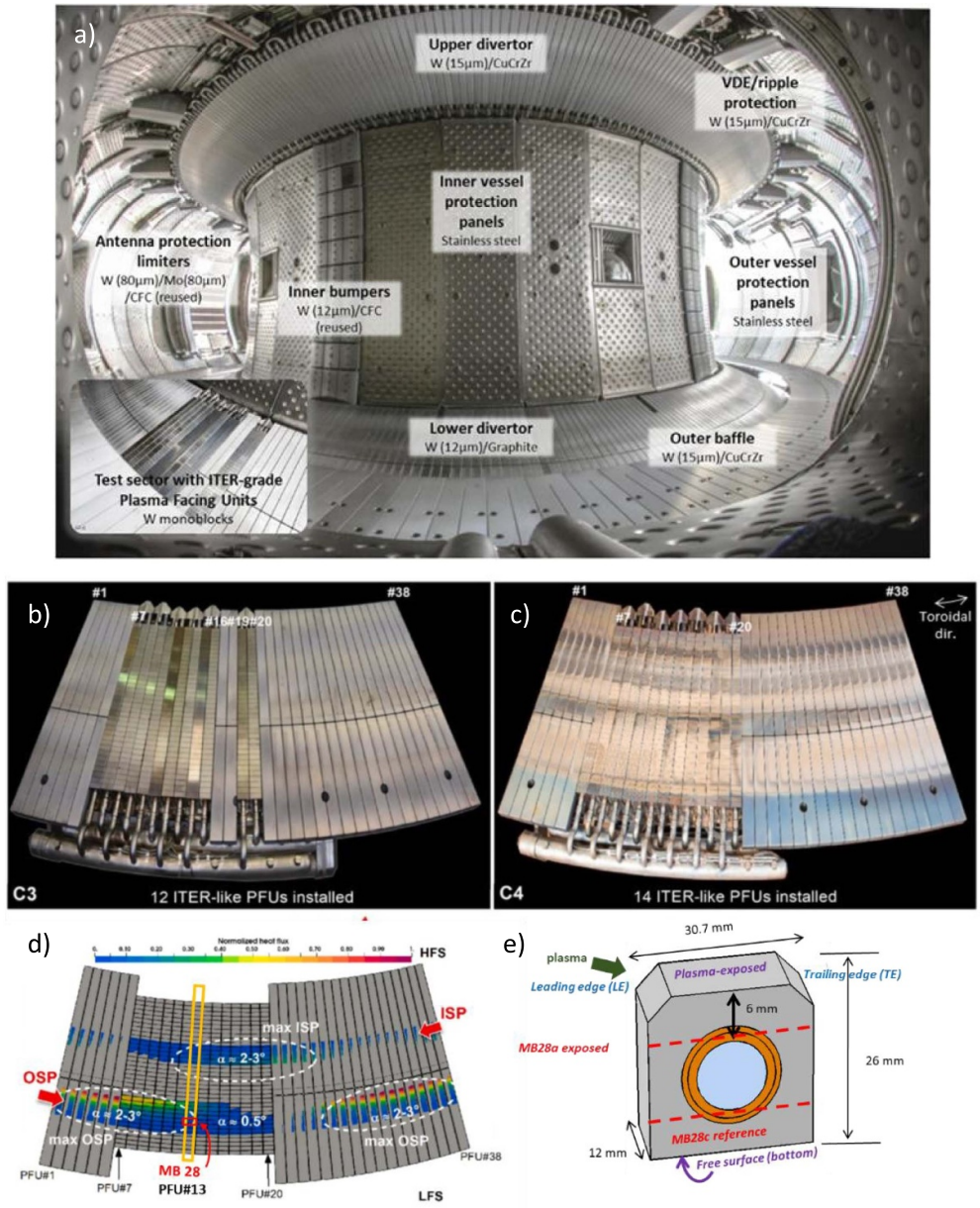

Figure 1. (*a*) Image of the interior of the WEST vacuum vessel, Reproduced from [16]. © EURATOM 2022. CC BY 4.0. Configuration of the lower divertor during (*b*) C3 and (*c*) C4 campaign; (*d*) the configuration of the divertor showing the heat load pattern, Reprinted from [17], Copyright (2023), with permission from Elsevier. (*e*) Schematic configuration of MB 28.

Table 1. Main parameters of the C3 and C4 experimental campaigns experienced by the MB 28 from PFU#13 under investigation.

	Plasma pulses	Cumulative time (s)	Disruptions	Deposited energy (MJ)	Boronizations
C3 July–December 2018	1076	7329	796	5052	3
C4–D2 July–November 2019	1112	9678	763	8962	5
C4–He October–November 2019	330	2991	279	4303	8

beam direction. Further details about the Tof-ERDA spectrometer (and the method) can be found in [47, 48]. Data analysis was performed using the Potku software [49]. Since the Tof-ERDA was performed after the NRA measurements, new spots were selected on the right side of the NRA spots, extending from the TE towards the leading edge (LE) direction. A total of nine spots were analyzed along the toroidal direction, spaced 3 mm apart, using a beam spot size of 2×3 mm^2.

It is noted that between successive measurements, the sample was maintained under vacuum.

3. Experimental results

An overview of the observed changes in MB 28, as assessed through optical microscopy and profilometry, is presented first, followed by the surface morphology including a detailed description of the microstructural features. The ion beam analysis and energy dispersive spectroscopy results on fuel retention and material migration are then discussed.

3.1. Overview and roughness

The optical image of the MB 28 surface after plasma exposure is presented in figure 2(*a*). It is evident that plasma exposure induces surface changes that vary along the toroidal direction, especially in the case of a misaligned MB, where the LE is more exposed to plasma than the TE.

The surface near the LE (0–4 mm) presents a light gray color. Between 4 and 15 mm from the LE, the surface turns dark gray. In the area extending from 15 to 24 mm the color of the surface becomes gradually lighter. Some scratches oriented parallel to the TE are also visible on the surface, especially near the TE. Additionally, black spots are observed in all areas, primarily consisting of carbon-rich areas. In figure 2(*a*), the different areas as identified from the optical image are marked by gray dotted lines, while the yellow dashed lines represent zones defined by integrating results from all employed techniques.

The surface roughness (Sa, areal roughness average) before and after plasma exposure, as determined by optical profilometry, is presented in figure 2(*b*). In the as-received state, the roughness is estimated as (0.50 ± 0.05) μm (see section 2.2.1). After exposure, it was measured all along the toroidal direction of the MB. Figure 2(*c*) depicts representative 2D optical profilometry maps at different distances from the LE, demonstrating the variation in roughness. Up to about 17 mm from the LE the plasma exposure (resulting in surface erosion and material deposition as it will be discussed in sections 3.2 and 3.3) has smoothed the surface roughness which varies between 0.32 and 0.42 μm (figures 2(*c*-i, ii)). The roughness between 19 and 23 mm from the LE is similar to that of the non-exposed MB and is caused by surface depressions (figure 2(*c*-iii). Near the TE, the roughness reaches its maximum (0.59 μm) due to scratches (figure 2(*c*-iv).

3.2. Surface morphology

This section presents the surface morphology of the various zones, along with the observed microstructural features, as investigated using SEM combined with EDX spectroscopy and optical profilometry with FIB cross-sectioning SEM. The zone definition, based on all results, is presented in figure 2(*a*) with yellow colored ranges.

Figure 3 shows backscattered electrons images of the different zones of the plasma exposed surface ((*a*)–(*d*)) as discussed in section 3.1 and (*e*) the reference sample. Figure 3(*f*) presents a secondary electron image of the reference sample. As reference sample, the free surface at the bottom of the MB (see figure 1(*a*)) has been used; this surface was not exposed to plasma. Cracks are visible on the surface of the untreated reference sample (figure 3(*e*)) which may have formed along the grain boundaries. It is noted that the mean grain size of the tungsten used in the MB (in the plane of the plasma exposure), is (57 ± 5) μm and the subgrain size of (1.1 ± 0.2) μm, as determined using the intercept method.

The features observed on the exposed surface include cracks (figure 3(*a*)), deposition areas (figure 3(*b*)), linear scratches/grooves oriented mainly parallel to the LE/TE (figures 3(*c*) and (*d*)) and elongated pointy objects (figure 3(*a*)) which will be described in more detail below.

3.2.1. Cracks. Cracks similar to those observed on the reference sample were detected in zones 1, 3 and 4 (figure 3). In zone 2 the cracks have been covered with deposition material. After the plasma exposure, additional cracks have been formed perpendicular to the LE (figure 4(*a*)), extending to the chamfered areas (figure 4(*c*)). Their maximum length is about 700 μm and their poloidal spacing is in the range of 250–300 μm (figure 4(*b*)). They are also formed along linear areas of high density adjacent elongated pointy objects (figure 4(*d*)). Additionally, in zone 1 small length cracks have been formed along the subgrain boundaries (figure 5), similar to those observed on the electropolished reference (not shown).

3.2.2. Formation of deposition areas. Minimum deposition of elements was observed on the surface of zone 1 (it will be discussed further in 3.3) and this is verified by the observation of cracks similar to those of the non-exposed sample (figures 3(*a*) and (*e*)). Unlike zone 1, zone 2 is mainly covered by B, N, O and Cu rich areas (figures 6(*b*), (*d*), (*e*) and (*g*)). Additionally, carbon-rich spots are distributed across the surface (figure 6(*c*)). Figure 7(*a*) shows a representative SEM image of zone 3 along with the corresponding elemental mappings for B, C, N, O, Fe, Cu and W. In this zone oxygen rich regions are predominantly formed along the linear areas (figure 7(*e*)). Spot analysis (not presented) shows that Cu, N and B are present in the area with deposition and absent in the green area (figure 7(*a*)). Carbon-rich spots were also observed (figure 7(*c*)).

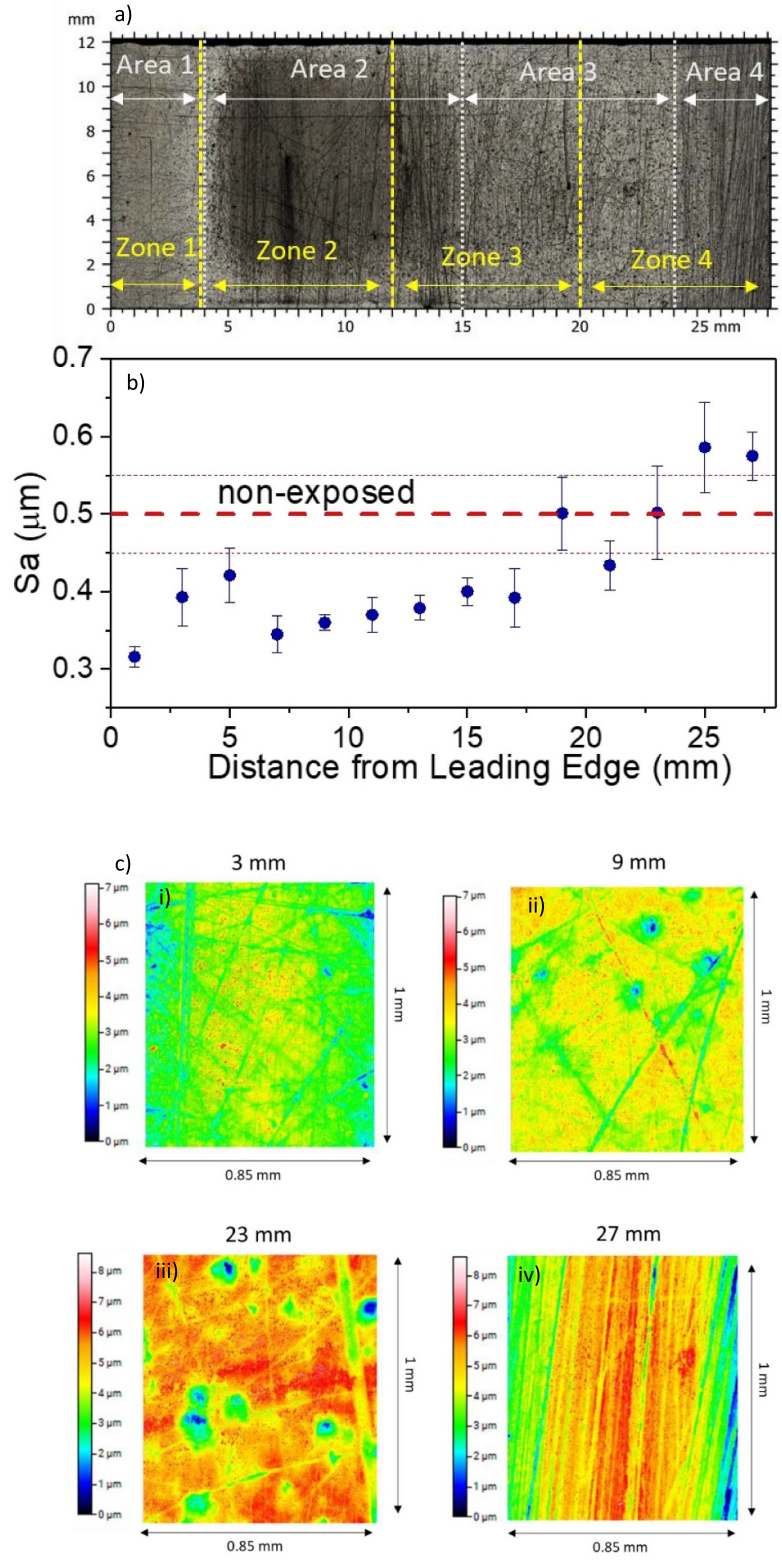

Figure 2. (*a*) Optical microscopy image of the MB 28 surface after plasma exposure; the gray dotted lines present the ranges of the different areas identified by the optical microscope, while the yellow dashed lines represent zones defined by integrating results from all employed techniques. (*b*) The roughness of the center area of the MBs (see 2.2.1) before plasma exposure (red dashed line) and along the toroidal direction after plasma exposure determined using optical profilometry (blue points). (*c*) 2D optical profilometry maps from each area at: (i) 3 mm, (ii) 9 mm, (iii) 23 mm and (iv) 27 mm from LE.

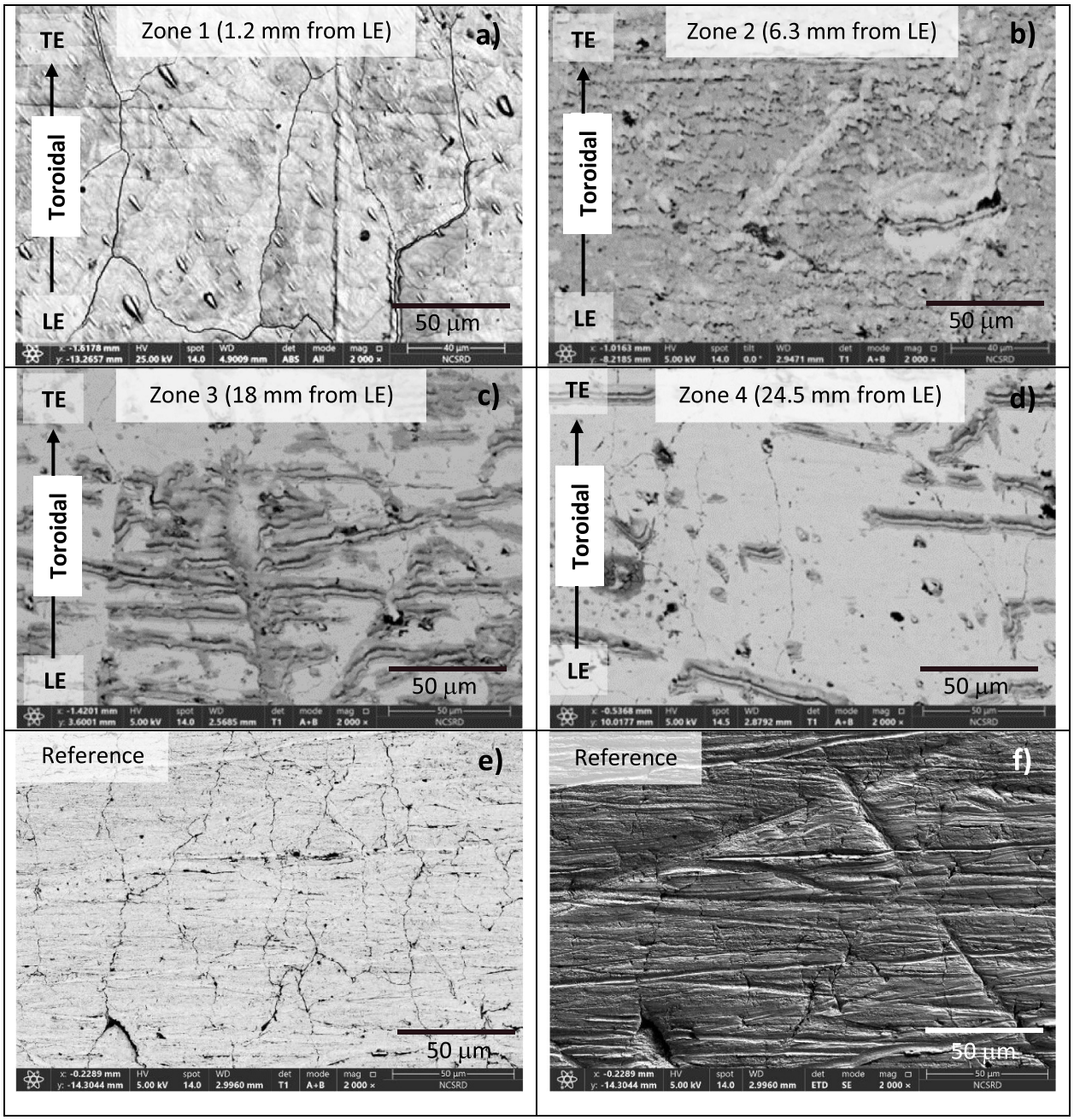

Figure 3. The backscattered electron images of (*a*) zone 1, (*b*) zone 2, (*c*) zone 3, (*d*) zone 4 of the plasma exposed surface and (*e*) the reference sample; (*f*) secondary electron image of the reference sample before the electropolishing.

Zone 4 displays linear deposition as shown by the dark gray areas in figure 3(*d*), though it is sparser compared to zone 3. In zone 4, near the TE edge, linear deposition parallel to the edge rich in B (figures 8(*c*)) and O (figure 8(*e*)) is observed along scratches (figures 8(*a*) and (*b*)). Areas rich in C (figure 8(*d*)) and spots rich in Cu (figure 8(*g*)) were also detected at these scratches. The Fe (figure 8(*f*)) distribution is similar to the W one (figure 8(*h*)).

The deposit grows in a characteristic manner, namely, it forms initially in areas of surface depression, in this case within scratches and spherical depressions (shadowed areas). With regard to scratches, however, it does not fill their interiors completely but builds up on one of the slopes and sometimes also at the slightly raised scratches' edges.

The areas of deposition are highly visible in the images recorded both in the surface topographic (SE) and compositional (BSE) modes. While the deposit present in the interior of the scratches is very distinctive, it is difficult to attribute, on the basis of SEM observations, the presence of irregularly shaped deposit-covered areas with the presence of depressions on the surface. Their presence was only revealed when the surface topography of the MB was examined using an optical profilometer.

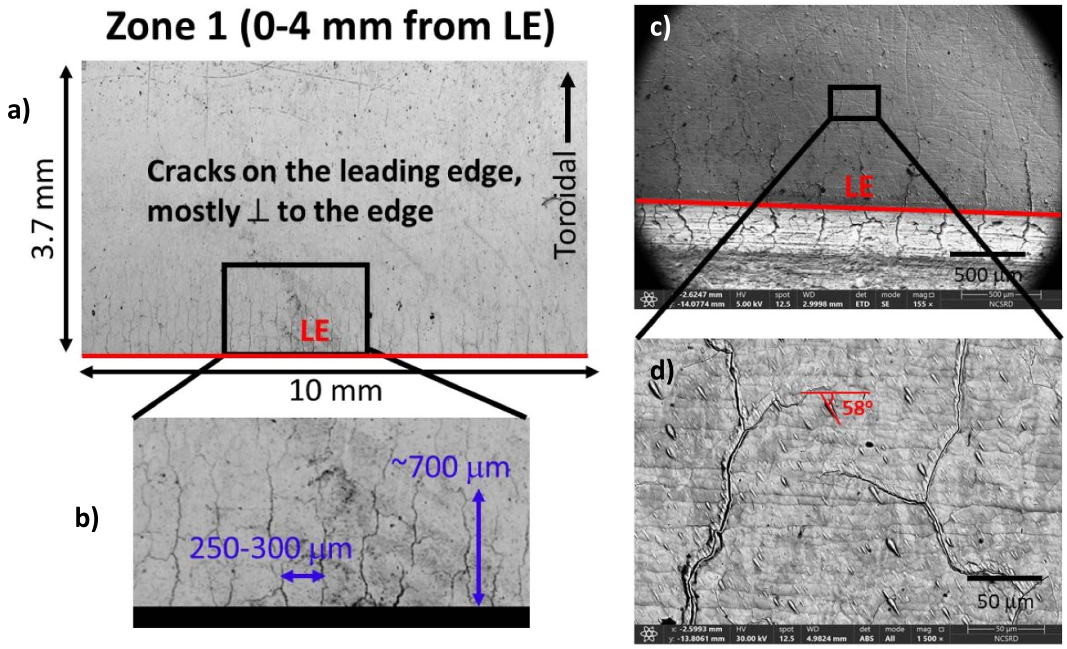

Figure 4. (*a*)–(*c*) Cracks vertical to the LE, (*d*) cracks along elongated pointy objects.

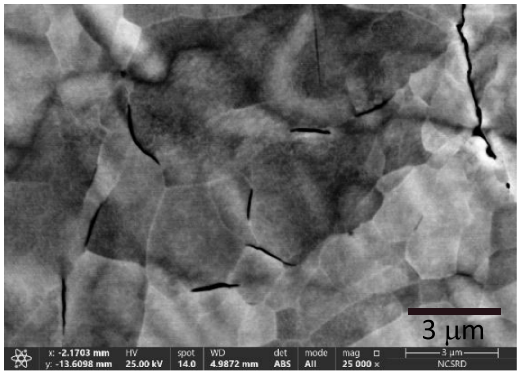

Figure 5. Cracks along the subgrain boundaries in the plasma exposed monoblock.

Figure 9 shows a summary image of the surface morphology registered by SEM, along with images of the same area recorded with an optical profilometer. It presents areas covered by deposit located both inside the scratches and inside the spherical depressions. The diameter of the largest depression is about 100 μm, and its depth is about 4.5 μm. Similar maps were recorded in the central part of the sample. They equally revealed the presence of shallow depressions with spherical morphology on the surface of the MB. It should be presumed that they were formed during the surface machining process/treatment of the MB.

In the images of the deposit registered by SEM and optical profilometer shown in figure 10, the layered structure of the deposit and its location with respect to the scratches can be clearly seen. In the area depicted in figure 10, the thickness of the deposit can be estimated at 0.6–0.7 μm, while the scratch depth at ∼0.6 μm. This value is comparable to the thickness of the deposit determined on the FIB cross-section taken on the slope of the scratch in the central part of the sample, being 0.85 μm at the widest point (figure 11, to be discussed further below). The recorded images confirm the shallowness of the scratches. They also provide insight into the structure of the deposit, which is layered and porous in places, with internal stratification/delamination, despite its small thickness.

The deposition pattern found in the MB is consistent with what was observed on the samples cut out from the WEST divertor erosion marker tiles [21], in which directional deposition in the form of longitudinal parallel lines was found.

3.2.3. Morphology and internal structure of elongated pointy objects. Elongated pointy objects, as shown in figure 3(*a*), are observed across the entire plasma exposed surface. These objects are oriented with their long axis at an angle of about 50°–60° relative to the LE/TE (see orientation in figures 3(*a*) and 12). The length of the long axis reaches up to 25 μm, with a length-to-width ratio ranging from 2 to 4. Each object presents a pointed tip directed towards the LE. Their number was estimated on the basis of analysis of images recorded at 500 and 1000 times magnification, for the central part of the MB. The obtained results oscillate in the range of 1000–3000 objects per mm^2. It is noted that in the areas where the objects are adjacent to each other (figure 4(*d*)) their number may be up to 10 times higher. In some cases, part of these objects (figure 12(*c*) and (*d*)) or the entire object (figure 12(*b*)) is missing, and in deposition zones, material accumulates around these objects (figure 12(*c*)).

FIB cross sections were carried out on two elongated pointy objects. On the cross-section of the former, two distinct areas

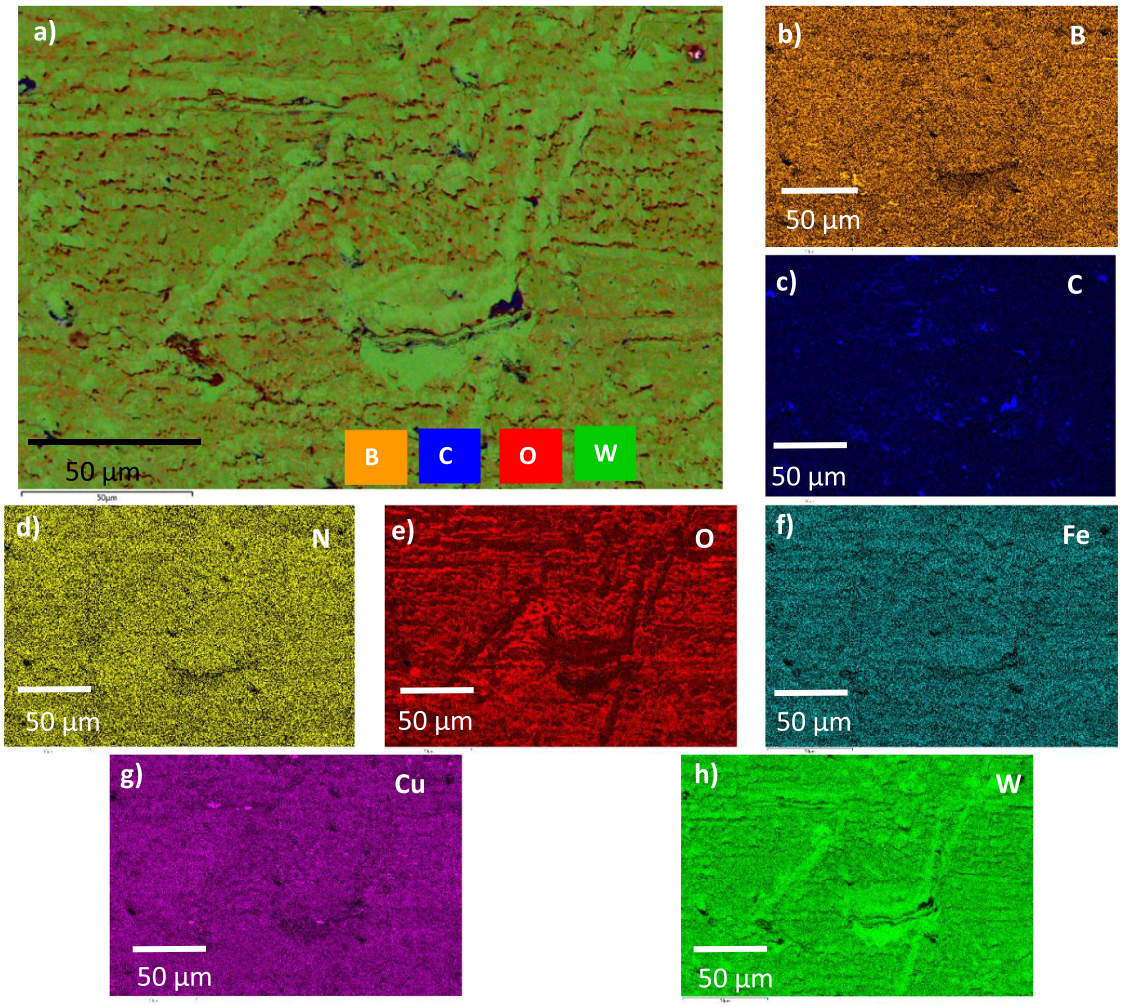

Figure 6. (*a*) SEM image from zone 2 and the corresponding elemental mapping of (*b*) B, (*c*) C, (*d*) N, (*e*) O, (*f*) Fe, (*g*) Cu and (*h*) W.

of layered structure are clearly visible (figures 13(*a*)–(*c*)). These areas are separated by a crack, and the directions of the layers in each area do not align (figure 13(*b*)). On cross-section of the latter, a layered build-up of deposit is observed on both sides of the chipping, which likely contained a dust particle. The layering directions in these regions also do not correspond with each other (figures 13(*d*)–(*f*)). Sub-layers of varying contrast and thickness are visible for both elongated pointy objects, differing in chemical composition. Porous areas are present, as well as stratification (figures 13(*c*) and (*f*)).

3.3. *Fuel retention and material deposition*

Figures 14(*a*) and (*c*) depict representative NRA experimental and simulated spectra, along with the elemental depth profiles (figures 14(*b*) and (*d*)) from a low deposition area (3 mm distance from the LE) and a high deposition one (9 mm distance from the LE), respectively. In the first zone, only carbon (*c*) and oxygen (O) (figure 14(*a*)) were detected and their deposition is restricted in a very thin layer with thickness of about 0.15 μm and a concentration of 6.5 at% and 19 at%, respectively (figure 14(*b*)). On the contrary, in the second zone (9 mm from the LE), a rich deposition is found. The detected elements are deuterium (*D*), boron (*B*), carbon (*C*), nitrogen (N) and oxygen (O) (figure 14(*c*)). The relevant nuclear reactions are denoted in figure 14(*c*). The deposition thickness is about 1.5 μm and the highest concentration of the detected elements is: 8 at% D, 35 at% B, 7.5 at% C, 10 at% N and 23 at% O. Fourteen areas, spaced 2 mm apart along the toroidal direction, were analyzed using NRA. The results will be discussed below, along with a comparison to those obtained through Tof-ERDA and EDX spectroscopy.

Nine points along the toroidal direction were analyzed using Tof-ERDA. Figure 15 shows the Tof-ERDA experimental spectra and depth profiles close to the sample surface (up to 1.5×10^{18} at cm^{-2} depth) for both the low deposition area (3 mm from the LE) and the high deposition area where maximum concentration of He was measured (6 mm from the LE). In all nine Tof-ERDA measured spots a strong surface peak of O was present.

Fourteen areas at a spacing of 2 mm along the toroidal direction were also analyzed using EDX spectroscopy. Figure 16 presents the EDX spectra from a) a low deposition area (3 mm from the LE) and b) a high deposition area (9 mm

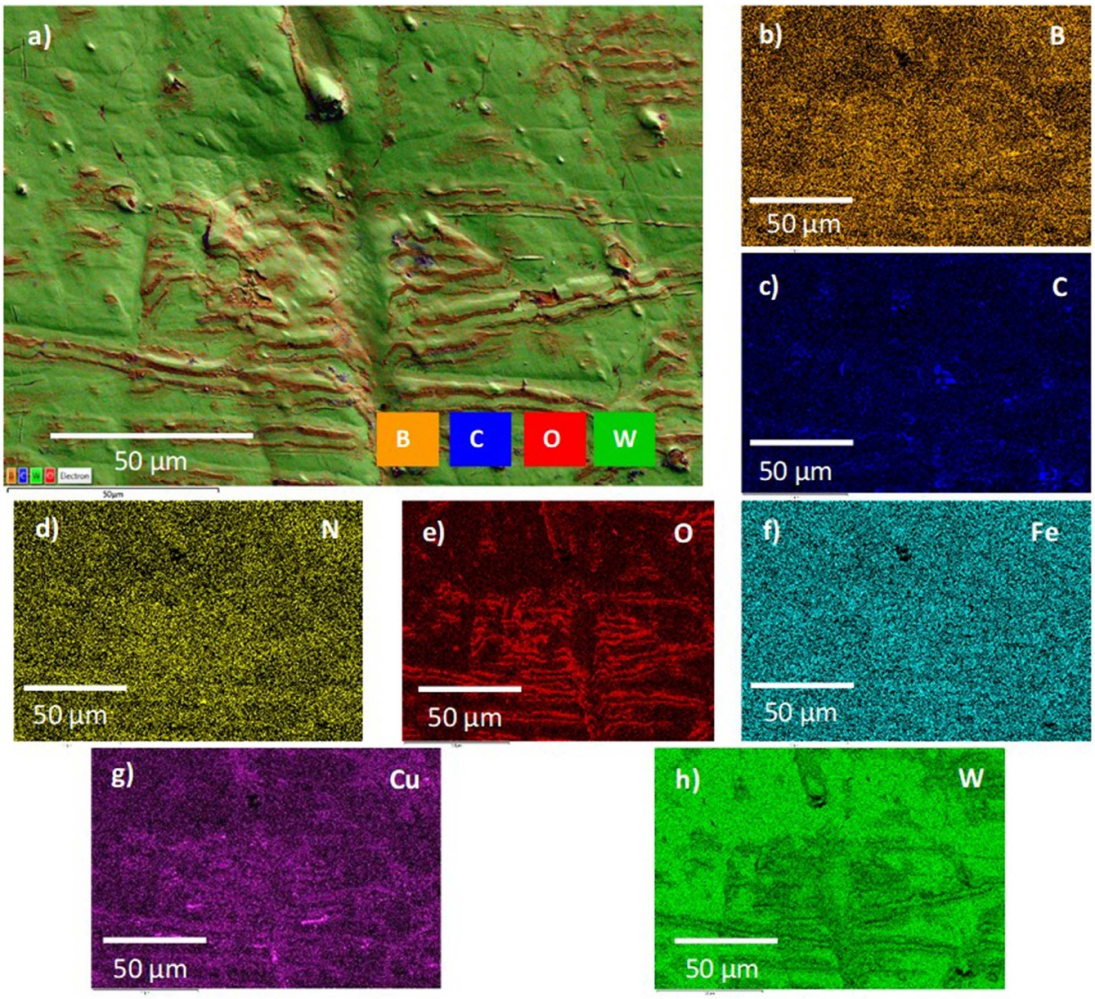

Figure 7. (*a*) SEM image from zone 3 and the corresponding elemental mapping of (*b*) B, (*c*) C, (*d*) N, (*e*) O, (*f*) Fe, (*g*) Cu and (*h*) W.

from the LE). In the former, the detected elements are C, N and O, while in the latter B, C, N, O, Fe, Cu and W were detected.

In figure 17 the concentration/amount of the detected elements using NRA, Tof-ERDA and EDX spectroscopy are depicted. The maximum detected depth for NRA is around 3 μm. The elemental concentrations in at% determined by Tof-ERDA correspond to the depth range of (40–120) nm. The elemental amount in at cm^{-2} presented in figures 17(*b*) and (*c*) for D and ^{4}He for Tof-ERDA were obtained from a layer with thickness of 0.24 μm. The elemental concentrations determined by EDX spectroscopy correspond to a surface layer with a thickness ranging from 70 nm in zone 1–170 nm in zones 2, as estimated from depth profiles obtained via NRA.

The amount of hydrogen (*H*), determined by Tof-ERDA, is almost constant along the toroidal direction, varying between 6.2 at% and 8.3 at%, apart from the point near the TE where it presents a much higher amount of (19.0 $\pm$ 1.3) at% (figure 17(*a*)). Deuterium (*D*) was detected by NRA and Tof-ERDA (figure 17(*b*)). The D amount, as determined by NRA, shows a sharp increase near the LE, peaking at about 7 mm from the LE before gradually decreasing towards the TE. Since the maximum analyzable depth using Tof-ERDA for the D amount is 1.5 $\times$ 10^{18} at cm^{-2}, the Tof-ERDA results for D content were scaled in order to be comparable with the NRA ones which correspond to a depth of 4 $\times$ 10^{18} at cm^{-2}. This scaling assumes a constant D concentration over the maximum detectable depth, which is valid to a first approximation as observed in figures 14(*d*), 15(*c*) and (*d*). The scaled Tof-ERDA data are presented in figure 17(*b*), and demonstrate good agreement with the NRA results, considering the following: In the NRA spectra the D(d,p$_0$)T peak overlaps with the ^{14}N(d,p$_5$)^{15}N one (figure 14(*c*)), which limits the accuracy in the determination of D amount by NRA. Figures 17(*a*) and (*b*) show that the deuterium concentration is higher than that of 1H.

The ^{4}He amount was determined by Tof-ERDA (figure 17(*c*)) and its distribution along the toroidal direction is similar to the deuterium one, presenting a peak of 0.92 $\times$ 10^{17} at cm^{-2} at the distance of 5 mm from the LE and then it decreases gradually to the values 0.15 $\times$ 10^{17} at cm^{-2} near the TE.

The concentration and amount of the deposited B, N, C and O as determined by NRA, Tof-ERDA and EDX

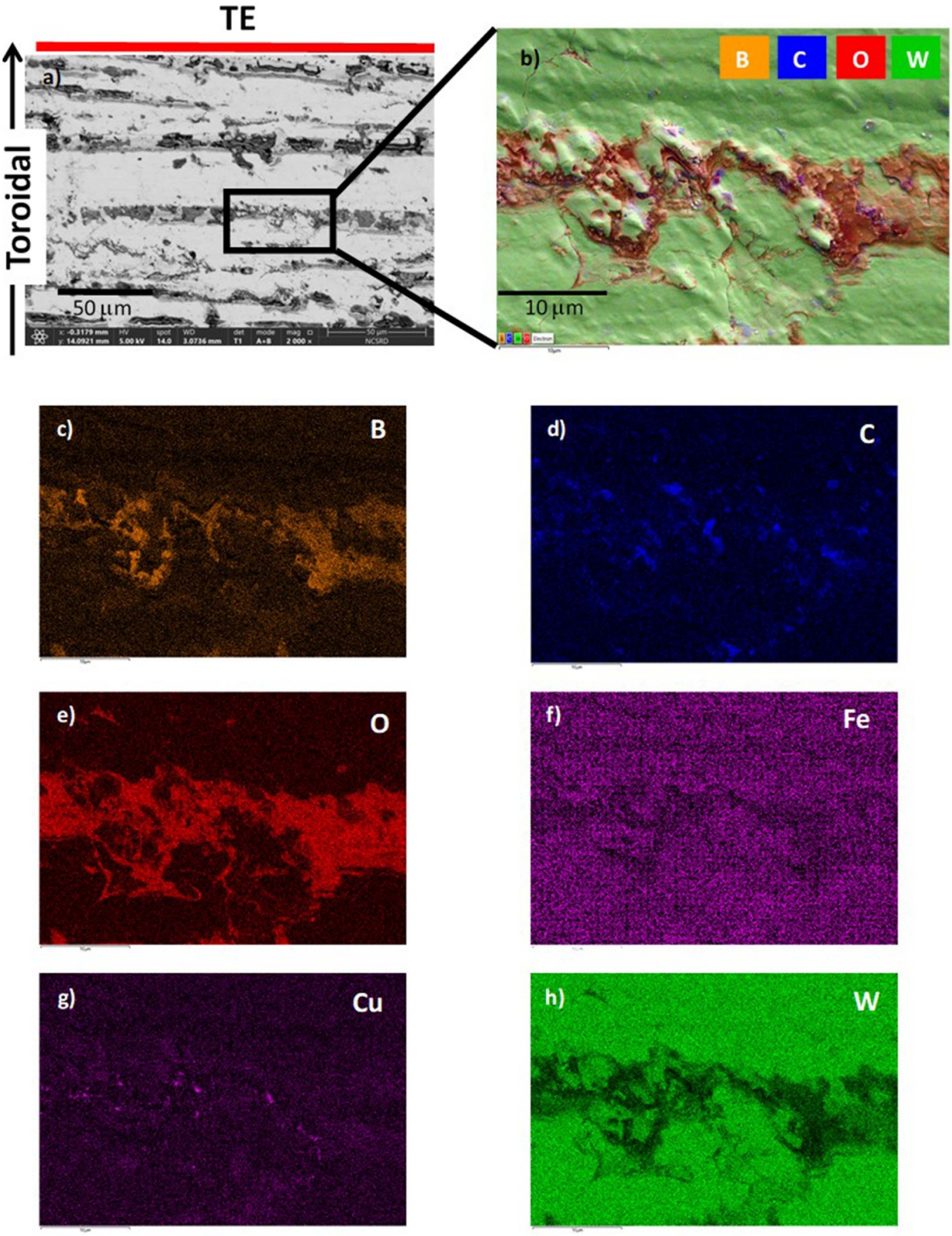

Figure 8. SEM image of a representative area in zone 4 near the TE and its elemental mapping.

spectroscopy is presented in figures 17(*d*)–(*g*), respectively. Good agreement among the three techniques is observed for the B and N distribution along the toroidal direction, taking into account the limitations of each technique and the different depths detected by each technique. B and N content present a peak at around 9 mm from the LE and it gradually decreases

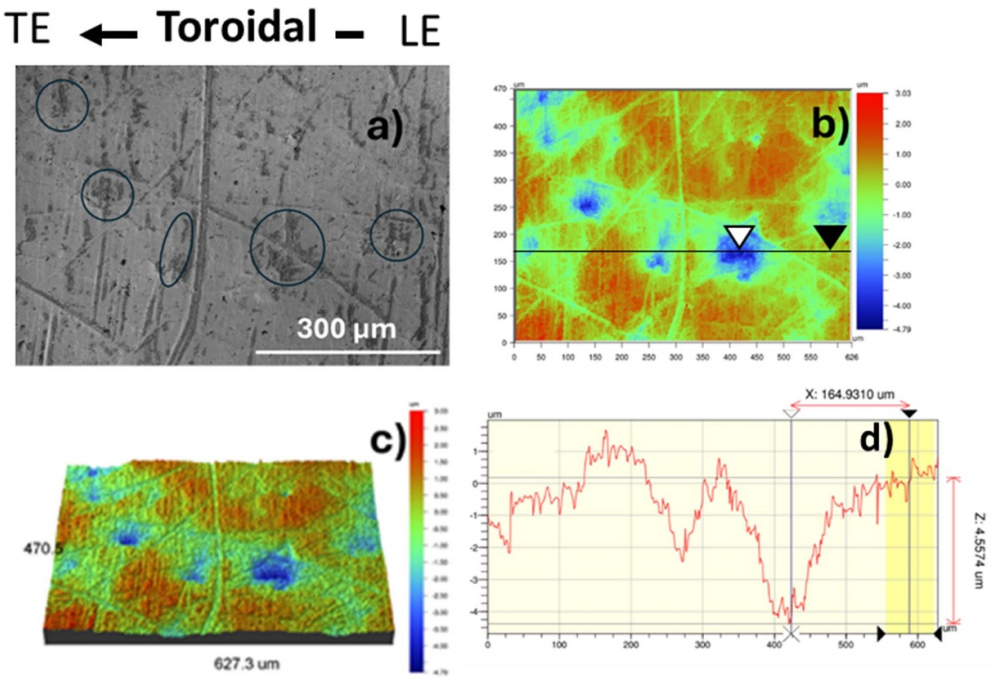

Figure 9. SEM image of (*a*) the deposit morphology together with (*b*) its 3D and (*c*) 2D maps and (*d*) its depth profile recorded with an optical profilometer. Location 23.5 mm from the LE.

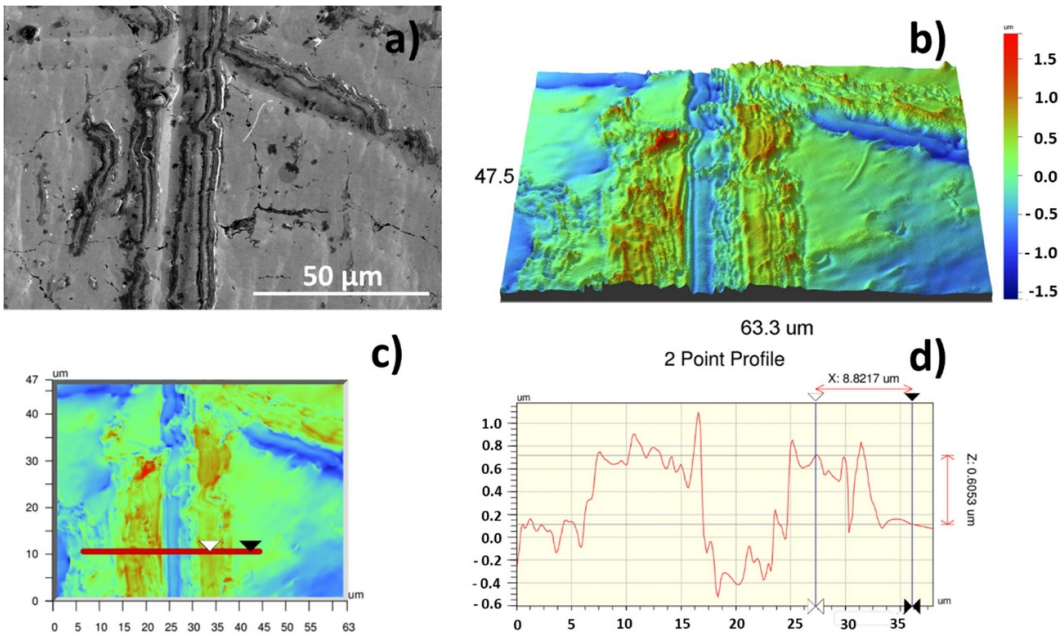

Figure 10. SEM image of the (*a*) deposit morphology together with (*b*) its 3D and (*c*) 2D maps and (*d*) its depth profile.

towards the TE. The maximum B amount is 2.2×10^{18} at cm^{-2} corresponding to a maximum concentration of about 30 at% according to Tof-ERDA and around 20 at% according to EDX (figure 17(*d*)). The maximum N amount is 2.8×10^{17} at cm^{-2} according to the NRA (figures 6(*f*)) and a maximum concentration of about 6 at% is found by both Tof-ERDA and EDX spectroscopy. C deposition (figure 17(*e*)) increases at the two edges, whereas in the middle region its amount fluctuates around the value of 3×10^{17} at cm^{-2}, corresponding to a concentration of about 5 at% as determined by Tof-ERDA. It is noted that EDX spectroscopy may overestimate the C content. For O deposition (figure 17(*g*)), NRA shows a peaking in its amount at 9 mm from the LE with its value varying in the range from 3×10^{17} to 11×10^{17} at cm^{-2}. Tof-ERDA shows that O concentration decreases gradually from the value of 20 at% close to the LE to 13 at% close to the TE. The discrepancy between Tof-ERDA and NRA regarding the O distribution along the toroidal direction is attributed to

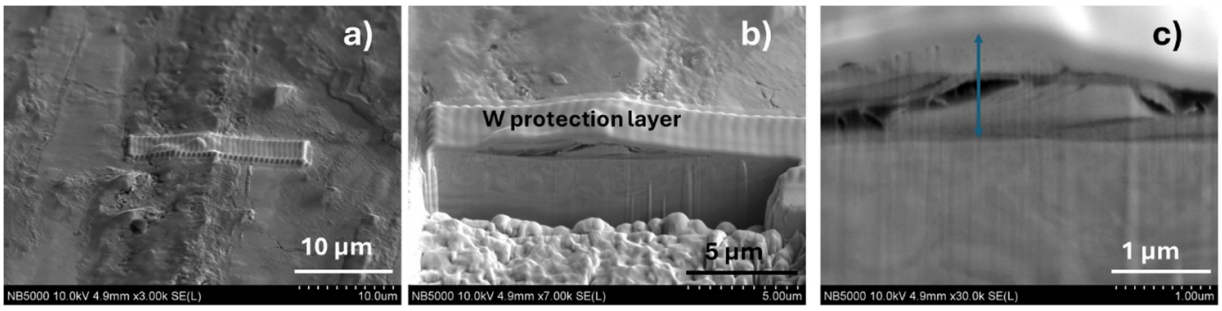

Figure 11. FIB registered SEM images of the deposit and its cross-sections, the central part of the monoblock. SEM images (*a*) before FIB was carried out, (*b*) after FIB and (*c*) after FIB with higher magnification, focusing on the cross section of the deposition.

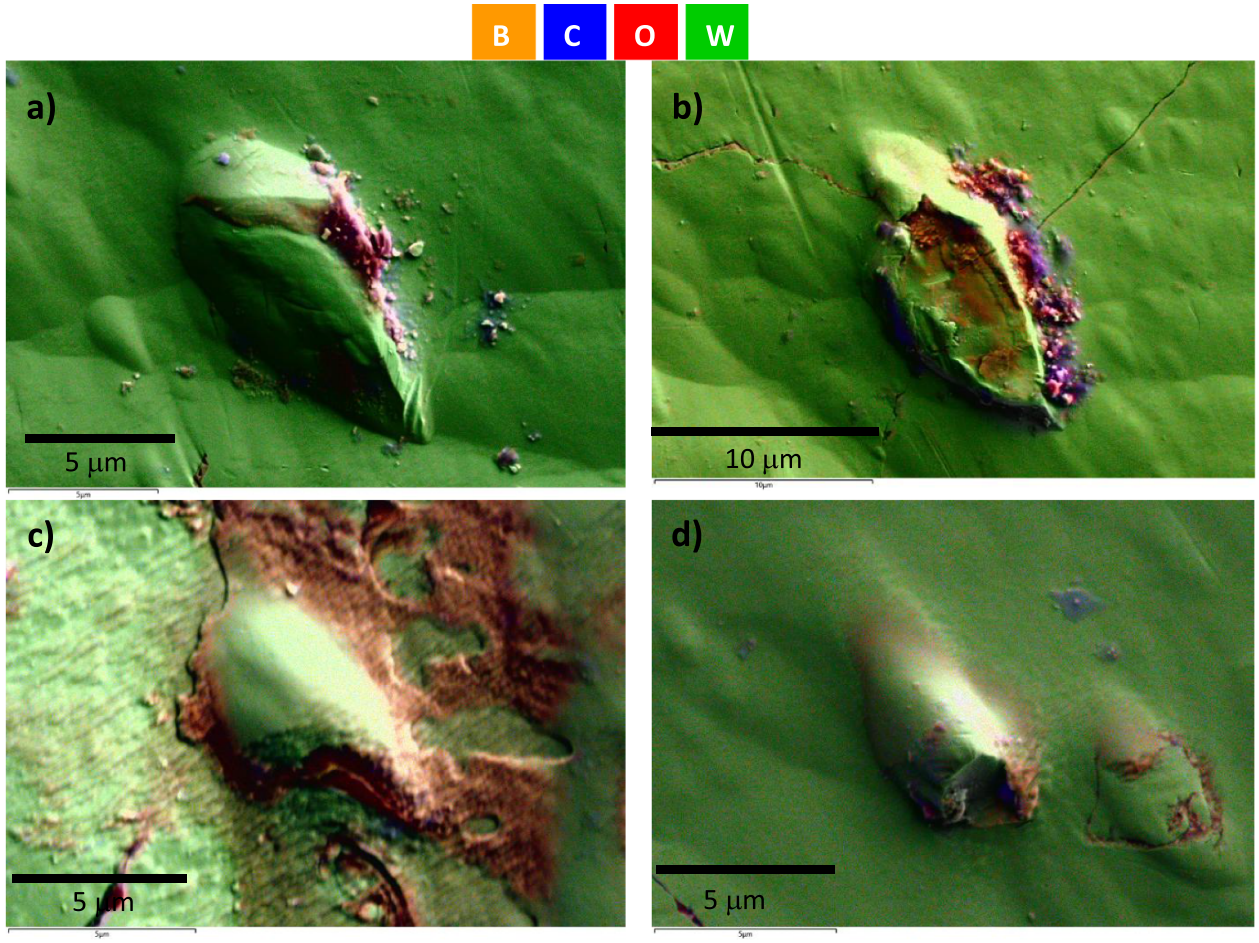

Figure 12. Top view of the pointy objects (*a*) as formatted (zone 1), (*b*) totally (zone 1) or partially removed from (*c*) zone 2 and (*d*) zone 4.

the different depths probed by each technique and to the limitations of each technique. Specifically, in the NRA spectra the end of the C peak overlaps with the O peak (figures 14(*a*) and 13(*c*)) which inhibits the accurate determination of oxygen.

Figure 17(*h*) shows the Fe and Cu concentrations as determined by EDX spectroscopy. Both elements exhibit similar distributions along the toroidal direction, with peak values of 3.3 at% for Cu and 2.2 at% for Fe at 9 mm from the LE. Figure 17(*i*) depicts the W concentration obtained using ToF-ERDA and EDX spectroscopy. The distributions are in good agreement, with differences in concentration at each point attributable to the presence of the other detected elements.

Based on the above discussed observations, we can redefine the four distinct zones according to the roughness, surface morphology, fuel retention and material deposition: 0 mm to 4 mm from the LE shows low deposition, 4 mm to 12 mm marks the highest deposition zone, 12 mm to 20 mm exhibits a smooth decrease in both material deposition and fuel retention, and 20 mm to 28 mm shows an increase in roughness while fuel retention and material deposition further decrease (figure 2(*a*) yellow dashed lines).

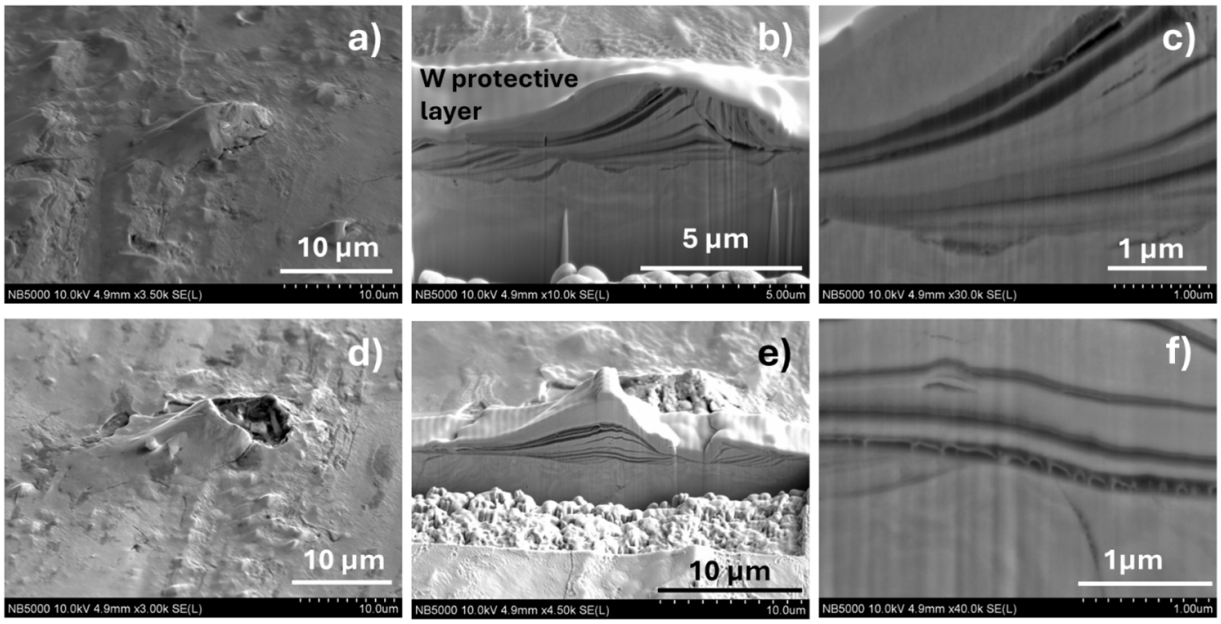

Figure 13. SEM images of the elongated pointy objects and their structure revealed on the FIB-produced cross-sections: (*a*)–(*c*) elongated pointy object no. 1 and (*d*)–(*f*) elongated pointy object no. 2.

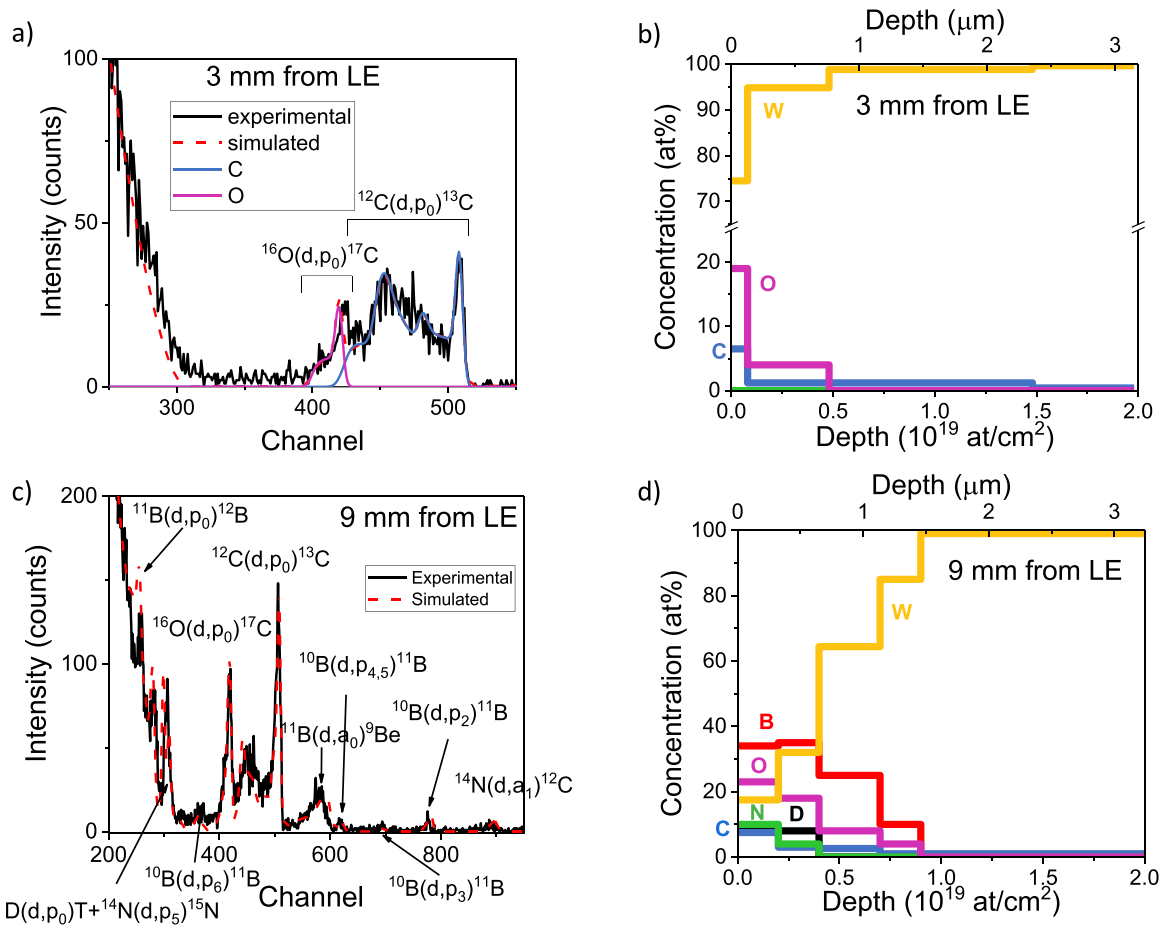

Figure 14. (*a*) NRA spectra of a low deposition area and (*b*) the corresponding elemental depth profiles; (*c*) NRA spectra of a high deposition area and (*d*) the corresponding elemental depth profiles.

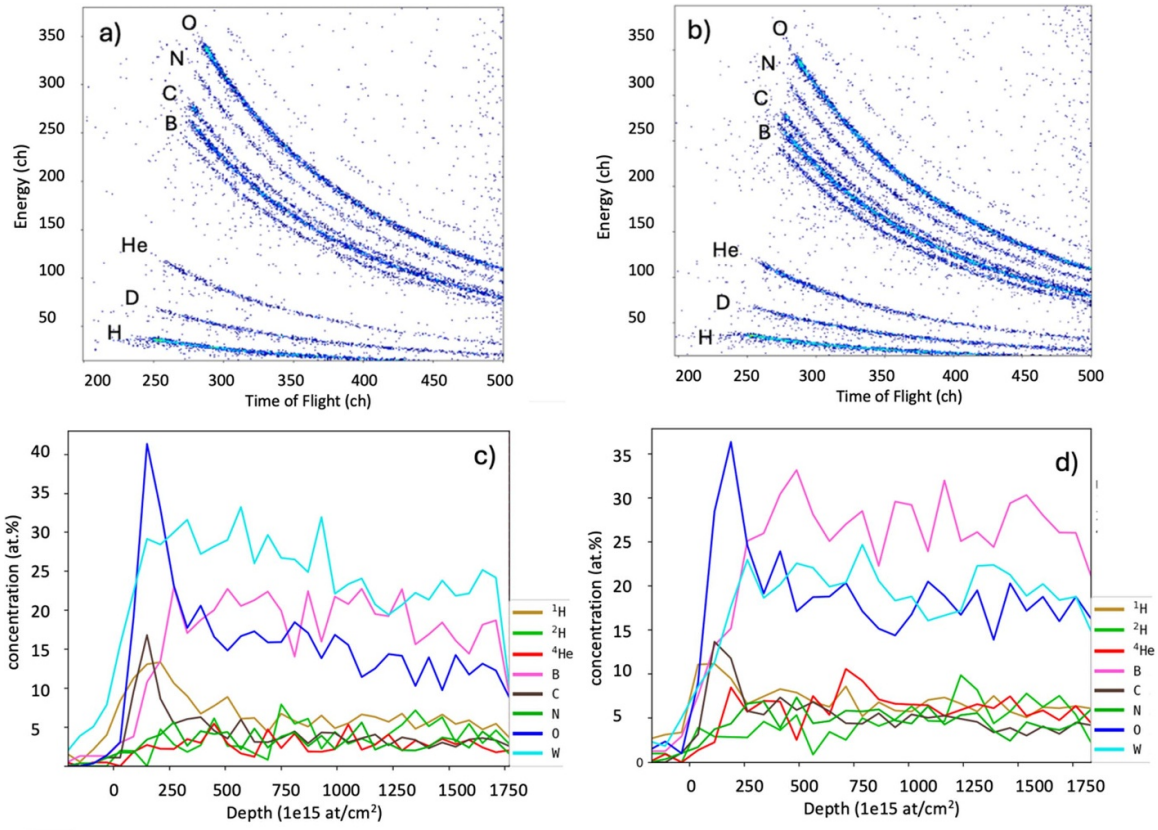

Figure 15. (*a*) Tof-ERDA spectrum of light elements (H–O) at the 3 mm position from the LE and (*c*) corresponding elemental concentrations (at%), (*b*) Tof-ERDA spectrum of light elements (H–O) from position 6 mm from LE and (*d*) corresponding elemental concentrations (at%).

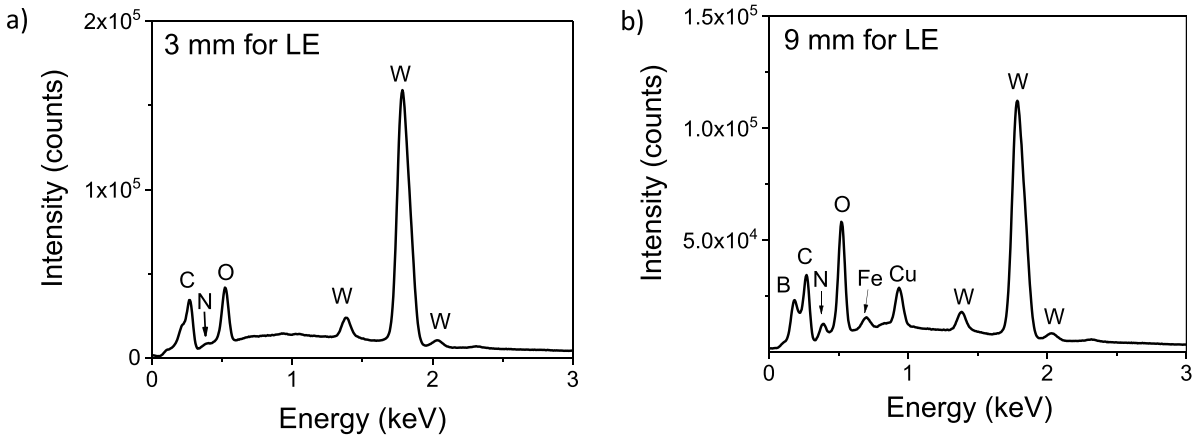

Figure 16. The EDX spectrum of (*a*) a low deposition area and (*b*) a high deposition area.

4. Discussion

The plasma exposed surface of the MB 28 can be divided into four distinct zones along the toroidal direction:

(a) **Zone 1 (0–4 mm from the LE)**: This zone appears light gray in color, with no scratches visible in SEM. It resembles the surface morphology of the electropolished reference sample and this is an indication that this zone has undergone erosion. Near the LE, cracks perpendicular to the edge have been developed. This phenomenon is not unique as these cracks were observed in 27% of all MBs and their causes are under investigation [50]. The deposition of B, N, Fe and Cu, as well as H/D retention is very low, while C deposition increases near the LE. The macroscopic roughness remains constant around 0.5 μm.

(b) **Zone 2 (4–12 mm from the LE)**: The transition from zone 1 to zone 2 is abrupt, marked by a color change from light to dark gray. This zone exhibits the highest material deposition (B, N, Fe and Cu) and fuel retention (D and ^{4}He). The

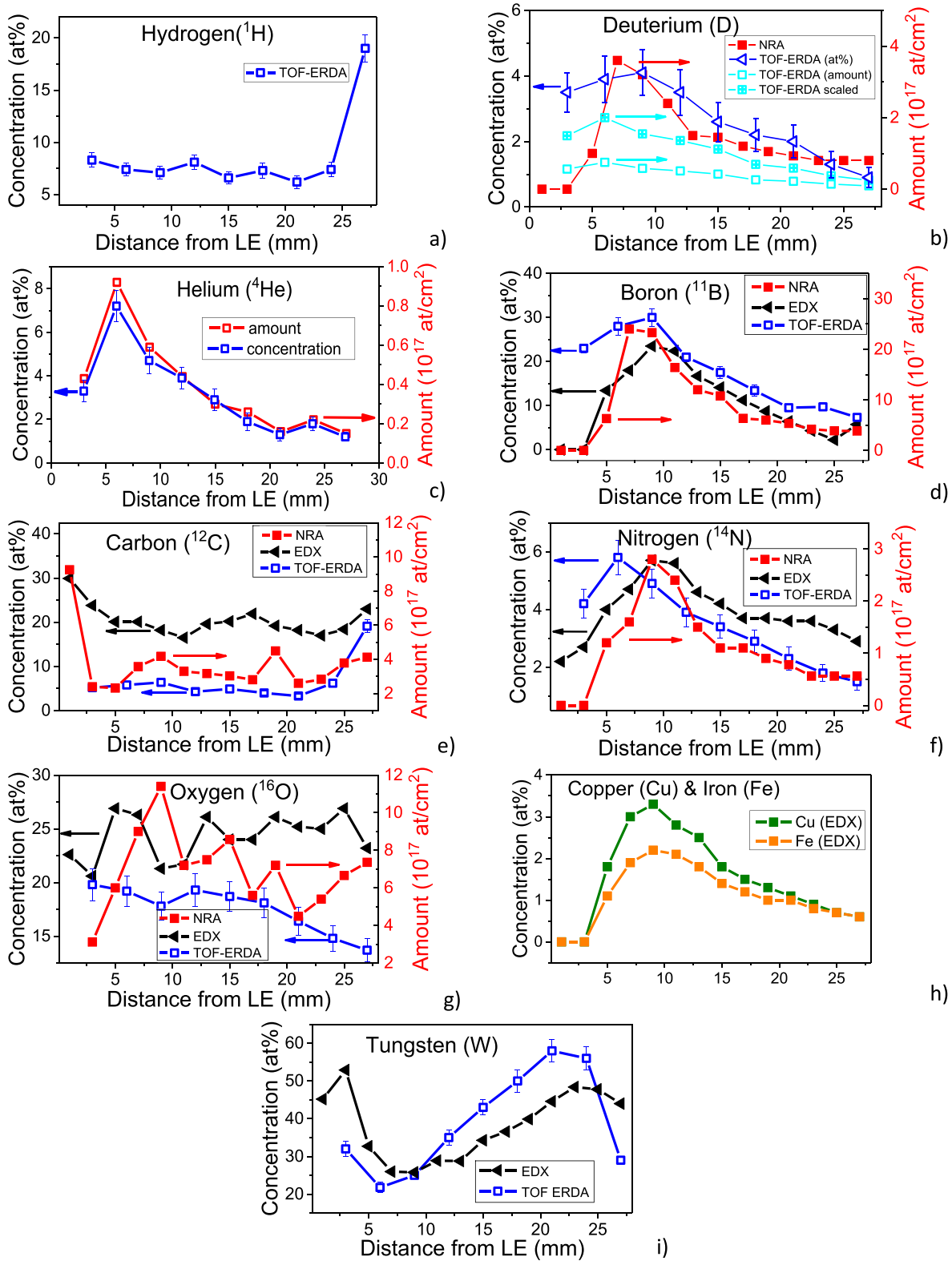

Figure 17. Elemental concentration along the toroidal distribution obtained by NRA, ToF-ERDA and EDX spectroscopy.

surface shows random scratches and black spots (mainly carbon rich areas), with almost the entire area covered by deposited material. The deposition layer thickness is approximately 1.5 μm. The surface roughness remains relatively low (0.5 μm), similar to that of zone 1.

(c) **Zone 3 (12–20 mm from the LE)**: In this zone, material deposition and fuel retention gradually decrease. The surface color lightens and dark spots persist. The deposition is now limited to linear areas and depressions. Cracks along the grain boundaries begin to reappear in non-deposition

areas. The roughness remains constant around 0.5 μm.

(d) **Zone 4 (20–28 mm from the LE)**: As the TE is approached roughness increases initially due to depressions followed by a further rise caused by scratches. The material deposition continues to decrease and the density of linear deposition areas diminishes. Cracks along the grain boundaries become more noticeable. The dense scratches parallel to the TE are rich in B and O.

The deuterium and helium plasma in C3 and C4 campaigns resulted in the deposition of D and He with maximum deposition of 3.6×10^{17} at cm^{-2} and 0.9×10^{17} at cm^{-2}, respectively, at approximately 6–7 mm from the LE. The boronization, using B_2H_6, which was performed 3 times during the C3 campaign and 13 times within the C4 campaign (table 1) with a total injected B amount of 192 g [51], for active wall conditioning and plasma performance improvement resulted in boron deposition varying between 10 and 30 at% along the toroidal direction. Carbon was also detected at a maximum concentration of about 30 at% (maximum amount of about 1×10^{18} at cm^{-2}) and its origin is attributed to (*a*) the W-coated graphite tiles (see figure 1(*a*)), (*b*) the W-coated carbon antenna protections (see figure 1(*a*)), (*c*) residual gas in the vacuum vessel, (*d*) oil diffusion pumps of the vacuum vessel, and (*e*) probably to sample handling. As the sputtering threshold energy predicted by theory and simulation for deuterium on W with carbon contamination is ∼85 eV, the C impurity in the sample can significantly enhance the sputtering yield of W [52, 53]. The maximum oxygen concentration was found 27 at% (maximum amount of 1.2×10^{18} at cm^{-2}) stemming mainly from outgassing of materials, plasma interaction with plasma facing components and residual gases in the vacuum system. It is noted that residual water in the vacuum system is a dominant oxygen source. It desorbs from walls, especially after venting or insufficient baking. Similarly to C impurity, O impurities in W also result in the reduction of the effective threshold energy of W–O mixed layer on W for sputtering by D ions leading to substantial increases in sputtering yields in the threshold energy region [52]. Maximum nitrogen deposition of about 6 at% (maximum amount of around 3×10^{17} at cm^{-2}) was detected and this originates from the exposure to air as there are always leaks in the vacuum vessel. Additionally, at the end of C4, nitrogen injections were performed for dedicated experiments. Small amounts of nitrogen were injected through the mid-plane for scenarios aimed at placing the X-point of the plasma on the upper divertor. It is unlikely that the nitrogen reached the lower divertor, but it remains a possibility [54]. Cu (from LH antennas, see figure 1(*a*)) and Fe (from steel panels, see figure 1(*a*)) impurities presenting a maximum concentration of about 3.3 at% and 2.2 at%, respectively, were detected. In a previous study [37] of various MBs of PFU #13, boron and tungsten carbides, tungsten borides and boron nitride have been found by x-ray photoelectron spectroscopy.

A correlation is generally observed between the deposition of B, N, Cu and Fe and the retention of D and ^{4}He.

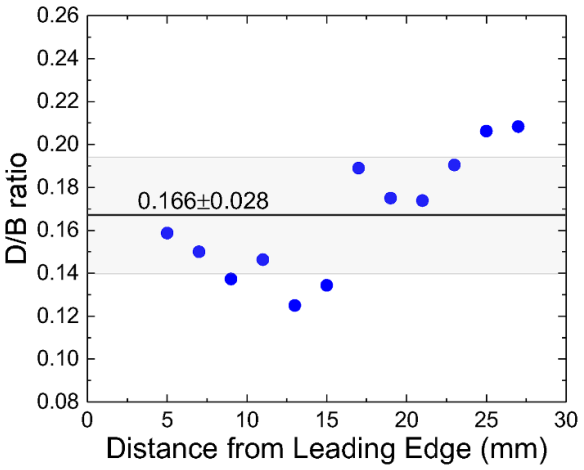

Figure 18. The D/B ratio determined by NRA along the toroidal direction.

However, the correlation between these elements and O deposition is more ambiguous. While both elemental mapping and Tof-ERDA data suggest a correlation, quantification via NRA and EDX spectroscopy does not support this conclusion. Additionally, the D/B ratio remains nearly constant of about 0.166 ± 0.028 along this direction (figure 18). This implies co-deposition of D and B. On the other hand, Tof-ERDA results indicate a clear correlation between C and ^{1}H deposition, suggesting the deposition in the form of hydrocarbons at the very surface (up to about 150 nm) of the deposited layers.

MB 28 exhibits nearly three times higher average D retention compared to the corresponding positions in the C4 IC PFU [18], likely due to thermal desorption effects at temperatures ranging from 900 °C to 1000 °C in the OSP of the IC PFU.

Oriented elongated objects are observed across the entire surface of the exposed sample. Cross-sectional analysis reveals that these features consist of a adhered dust particle embedded in a stratified structure formed on the sample surface. In some cases, the deposited particle has remobilized, leaving a crater in the feature. Additionally, material deposition was observed around these features. The mechanism of formation of similar objects was explained in [55] which refers to an experiment with a polished tungsten specimen exposed to the outer divertor plasma of ASDEX Upgrade close to the strike point. It describes that a deposit can form around dust particles adhered on a surface; in our study this might be the case, including the deposition also at surface irregularities.

The region of the examined monoblock (MB 28) on the PFU is characterized as eroded in previous studies [17, 37]. However, the results of the present study indicate that the sample experienced distinct phenomena along the toroidal direction, with millimeter-scale morphological variations. The observed pattern of the erosion, material deposition and fuel retention along with the morphological changes were caused by heat and particle fluxes that follow the magnetic field lines, impacting PFCs at grazing angles in combination with the poloidal misalignment of MB 28 during C4. Small variations in magnetic topology lead to strongly localized heat loads. In the

OSP region, this naturally produces toroidal asymmetries in power deposition.

5. Summary and conclusions

The erosion-deposition profile along the toroidal direction and the surface morphology of the plasma exposed MB 28 were investigated using NRA, Tof-ERDA, SEM with EDX spectroscopy, FIB cross-sectioning SEM and optical profilometry.

Starting from the LE, low material deposition (boron, nitrogen, copper and iron) and fuel (deuterium and helium) retention were observed. The surface close to the LE appears to have undergone erosion, presenting a grain structure similar to that of the reference sample. However, additional cracks, perpendicular to the LE, have been formed due to plasma exposure; they present a poloidal spacing of 250–300 μm and a maximum length of 700 μm.

The crack formation on the LE is most probably related to the increase of the surface temperature at the chamfered poloidal edge above the ductile to brittle transition temperature of tungsten as discussed in [17]. The temperature of MB 28 was not monitored by the VHR IR camera; however, its neighboring MB, MB 27 (PFU #13), was monitored (see figure 5(*b*) of [50]). Because of the vertical misalignment mentioned (see introduction) there is a temperature gradient in steady state along the toroidal direction, i.e. 500–900 °C on the LE versus 300 °C on the rest of the MB. During disruptions the temperature can go even higher (>1000 °C). According to modelling studies, in the case of misaligned MBs during disruptions the temperature at the poloidal edge can rise above 1000 °C, even up to the recrystallization temperature of W (1400–1500 °C) leading to brittle fracture [32].

At approximately 4 mm from the LE, material deposition and fuel retention increase sharply, peaking between 6 and 10 mm, with maximum deposition thickness of about 1.5 μm. Beyond this point, both deposition and retention gradually decrease towards the TE. Deposition and fuel retention are preferentially concentrated along linear grooves and depressions. In the highest deposition and retention zone, the density of linear features increases, covering the majority of the area. Generally, there is a correlation among the boron, nitrogen, copper and iron deposition and fuel retention, while the C deposition is correlated with the H deposition for depths up to about 120 nm.

Additionally, oriented elongated objects were observed across the entire surface of MB 28. These objects consist of a stratified structure with, in some cases, embedded dust particles. Similar features have been observed in ASDEX Upgrade and WEST divertor marker tiles.

While previous studies identified the region of MB 28 on the PFU as eroded [17, 37], our results demonstrate significant variability in the toroidal direction, around the strike point, manifested as millimeter-scale morphological changes and detailed material deposition patterns obtained by ion beam analyses. Re-deposition of eroded tungsten and other impurities results in spatially heterogeneous surface modifications, including roughening, nano-structuring, and crack formation over characteristic length scales of ∼28 mm. These observations highlight the highly localized nature of PWIs, which are strongly influenced by surface temperature, impurity content, and component alignment.

Post-mortem analyses of additional ITER-like actively cooled PFUs are currently underway, and the resulting data will be used to consolidate the experimental database supporting PWI modeling for ITER and future fusion devices. WEST is currently in an advanced operational campaign (2025) focused on long-pulse plasma physics and materials testing with actively cooled tungsten divertors. Following this campaign, a planned technical shutdown will enable inspection and preparation for subsequent experiments in 2026.

Acknowledgment

This work has been carried out within the framework of the EUROfusion Consortium, funded by the European Union via the Euratom Research and Training Programme (Grant Agreement No. 101052200—EUROfusion). Views and opinions expressed are however those of the author(s) only and do not necessarily reflect those of the European Union or the European Commission. Neither the European Union nor the European Commission can be held responsible for them. The funding from the Hellenic General Secretariat for Research and Innovation for the Greek National Programme of the Controlled Thermonuclear Fusion is acknowledged.

ORCID iDs

K. Mergia 0000-0002-2633-8750
E. Fortuna-Zaleśna 0000-0002-1090-1641
C. Martin 0000-0002-4704-3273
D. Papadakis 0000-0002-9357-8252

References

[1] Pitts R.A. *et al* 2005 Material erosion and migration in tokamaks *Plasma Phys. Control. Fusion* **47** B303–22
[2] Federici G. *et al* 2001 Plasma-material interaction in the current tokamaks and their implications for the next step fusion reactors *Nucl. Fusion* **41** 1967
[3] Roth J. *et al* 2009 Recent analysis of key plasma wall interactions issues for ITER *J. Nucl. Mater.* **390–1** 1–9
[4] Hirai T. *et al* 2013 ITER tungsten divertor design development and qualification *Fusion Eng. Des.* **88** 1798–801
[5] Pitts R.A. *et al* 2025 Plasma-wall interaction impact of the ITER re-baseline *Nucl. Mater. Energy* **42** 101854
[6] Pintsuk G. 2012 Tungsten as a plasma-facing material *Compr. Nucl. Mater.* **4** 551–81
[7] Wu C.H. and Mszanowski U. 1995 A comparison of lifetimes of beryllium, carbon, molybdenum and tungsten as divertor armour materials *J. Nucl. Mater.* **218** 293–301
[8] Brezinsek S. *et al* 2013 Fuel retention studies with ITER-Like Wall in JET *Nucl. Fusion* **53** 083023
[9] Schmid K. and Wauters T. 2024 Full W ITER: assessment of expected W erosion and implications of boronization on fuel retention *Nucl. Mater. Energy* **41** 101789
[10] Zohm H. *et al* 2024 Overview of ASDEX upgrade results in view of ITER and DEMO *Nucl. Fusion* **64** 112001

[11] Pamela J., Matthews G.F., Philipps V. and Kamendje R. 2007 An ITER-like wall for JET *J. Nucl. Mater.* **363–5** 1–11

[12] Missirlian M. *et al* 2014 The WEST project: status of the ITER-like tungsten divertor *Fusion Eng. Des.* **89** 1048–53

[13] Firdaouss M. *et al* 2017 Overview of the different processes of tungsten coating implemented into WEST tokamak *Fusion End. Des.* **124** 207–2010

[14] Kwon S. *et al* 2025 Engineering evaluation of the upgrade KSTAR divertor system *Fusion Eng. Des.* **216** 115100

[15] Krieger K. *et al* 2025 Scrape-off layer and divertor physics: chapter 5 of the special issue: on the path to tokamak burning plasma operation *Nucl. Fusion* **65** 043001

[16] Bucalossi J. *et al* 2022 Operating a full tungsten actively cooled tokamak: overview of WEST first phase of operation *Nucl. Fusion* **62** 042007

[17] Diez M. *et al* 2023 Overview of plasma-tungsten surfaces interactions on the divertor test sector in WEST during the C3 and C4 campaigns *Nucl. Mater. Energy* **34** 101399

[18] Balden M. *et al* 2021 Erosion and redeposition patterns on entire erosion marker tiles after exposure in the first operation phase of WEST *Phys. Scr.* **96** 124020

[19] Hakola A. *et al* 2021 Gross and net erosion balance of plasma-facing materials in full W tokamaks *Nucl. Fusion* **61** 116006

[20] Jogi I., Paris P., Bernard E., Diez M., Tsitrone E., Hakola A., Likonen J., Vuoriheimo T. and Grigore E. 2023 Ex situ LIBS analysis of WEST divertor wall tiles after C3 campaign *J. Nucl. Eng.* **4** 96–100

[21] Hakola A. *et al* 2025 Evolution of elemental depth profiles on co-deposited layers at the divertor region of the WEST tokamak during its Phase 1 operations *Nucl. Mater. Energy* **45** 101998

[22] Richou M. *et al* 2022 First plasma exposure of a pre-damaged ITER-like plasma-facing unit in the WEST tokamak: procedure for the FPU preparation and lessons learned *Nucl. Fusion* **62** 056010

[23] Corre Y. *et al* 2023 Plasma exposure of a pre-damaged ITER-like plasma facing unit in the WEST tokamak: *in-situ* and post-mortem measurements *Nucl. Mater. Energy* **34** 101366

[24] Diez M., Gunn J.P., Firdaouss M., Grosjean A., Corre Y., Delmas E., Gargiulo L. and Tsitrone E. 2020 First evidence of optical hot spots on ITER-like plasma facing units in the WEST tokamak *Nucl. Fusion* **60** 0540001

[25] Fedorczak N. *et al* 2021 Cross diagnostics measurements of heat load profiles on the lower tungsten divertor of WEST in L- mode experiments *Nucl. Mater. Energy* **27** 100961

[26] Gaspar J. *et al* 2021 Divertor power loads and scrape off layer width in the large aspect ratio full tungsten tokamak WEST *Nucl. Fusion* **61** 096027

[27] Corre Y. *et al* 2023 Testing of ITER-grade plasma facing units in the WEST tokamak: progress in understanding heatloading and damage mechanisms *Nucl. Mater. Energy* **37** 101546

[28] Tichit Q. *et al* 2025 Plasma heat load in the toroidal gaps of the ITER-like plasma facing units in WEST tokamak *Nucl. Mater. Energy* **42** 101899

[29] Grosjean A. *et al* 2020 First analysis of the misaligned leading edges of ITER-like plasma facing units using a very high resolution infrared camera in WEST *Nucl. Fusion* **60** 106020

[30] Grosjean A. *et al* 2023 Very high-resolution infrared imagery of misaligned tungsten monoblock edge heating in the WEST tokamak *Nucl. Mater. Energy* **37** 101546

[31] Gunn J.P. *et al* 2021 Thermal loads in gaps between ITER divertor monoblocks: first lessons learnt from WEST *Nucl. Mater. Energy* **27** 100920

[32] Durif A., Richou M., Bergheau J.-M., Corre Y., Diez M., Reilhac P., Gunn J.P. and Tsitrone E. 2023 Edge cracking of WEST tungsten actively cooled plasma facing components after plasma operation *Fusion Eng. Des.* **188** 113441

[33] Corre Y. *et al* 2021 Sustained W-melting experiments on actively cooled ITER-like plasma facing unit in WEST *Phys. Scr.* **96** 124057

[34] Gaspar J. *et al* 2019 Emissivity measurement of tungsten plasma facing components of the WEST tokamak *Fusion Eng. Des.* **149** 111328

[35] Gasper J. *et al* 2020 In-situ assessment of the emissivity of tungsten plasma facing components of the WEST tokamak *Nucl. Mater. Energy* **25** 100851

[36] Fedorczak N., Gaspar J., Firdaouss M., Moncada V., Grosjean A., Dejarnac R., Brezinsek S., Tsitrone E., Bucalossi J. and Loarer T. 2020 Infra-red thermography estimate of the deposited heat load dynamics on the lower tungsten divertor of WEST *Phys. Scr.* **T171** 014046

[37] Marin A., Saefan A., Unterberg E., Parish C.M., Bernard E., Diez M., Tsitrone E. and Wang X. 2025 XRS post-mortem analysis of plasma-facing units extracted from WEST after the C3 (2018) and C4 (2019) campaigns *J. Nucl. Mater.* **604** 155525

[38] Diez M. *et al* 2021 In situ observation of tungsten plasma-facing components after the first phase of operation of the WEST tokamak *Nucl. Fusion* **61** 106011

[39] Tsitrone E. *et al* 2022 Investigation of plasma wall interactions between tungsten plasma facing components and helium in the WEST tokamak *Nucl. Fusion* **62** 076028

[40] Lasa A. *et al* 2024 Multi_physics modelling of tungsten collector probe samples during the WEST C4 He campaign *Nucl. Fusion* **64** 106012

[41] KLA Corporation, Filmetrics Profilm3D Optical Profiler [Apparatus], Milpitas, CA, USA (available at: www.filmetrics.com/profilometers/profilm3d)

[42] Gurbich A.F. 2016 SigmaCalc recent development and present status of the evaluated cross-sections for IBA *Nucl. Instrum. Methods B* **371** 27–32

[43] Kokkoris M., Diakaki M., Misaelides P., Aslanoglou X., Lagoyannis A., Raepsaet C., Foteinou V., Harissopulos S., Vlastou R. and Papadopoulos C.T. 2009 Study of the d+11B system differential cross-sections for NRA purposes *Nucl. Instrum. Methods B* **267** 1740–3

[44] Kokkoris M., Foteinou V., Provatas G., Kontos A., Patronis N., Papadopoulos C.T., Vlastou R., Misaelides P., Lagoyannis A. and Harissopulos S. 2007 A detailed study of the d + ^{10}B system for nuclear reaction analysis—part A: the ^{10}B(d, p)^{11}B reaction in the energy region $E_{d,lab}$=900-2000 keV *Nucl. Instrum. Methods B* **263** 357–68

[45] Gruebler W., Konig V., Schelzbach P.A., Jenny B. and Vybiral J. 1981 New highly excited ^{4}He levels found by the ^{2}H(d, p)^{3}H *Nucl. Phys.* **369** 381–295

[46] Tsavalas P., Mergia K., Lagoyannis A., Papadakis D., Diez M., Martin C. and The WEST Team 2024 Post-mortem analysis of the erosion/deposition pattern on ITER-like W-monoblock from the WEST divertor 26th *Int. Conf. on Plasma Surface Interaction in Controlled Fusion Devices* (*Marseille, France*, *12–17 May 2024*) (available at: https://irfm.cea.fr/en/evenement/26th-psi-conference/)

[47] Siketic Z., Radovic I.B. and Jaksic M. 2008 Development of a time-of-flight spectrometer at the Ruđer Bošković Institute in Zagreb *Nucl. Instrum. Methods B* **266** 1328–32

[48] Siketic Z., Skukan N. and Radovic I.B. 2015 A gas ionisation detector in the axial (Bragg) geometry used for the time-of-flight elastic recoil detection analysis *Rev. Sci. Instrum.* **86** 083301

[49] Arstila K. *et al* 2014 Potku—new analysis software for heavy ion elastic recoil detection analysis *Nucl. Instrum. Methods B* **331** 34–41
[50] Diez M. *et al* 2024 Experimental characterization of leading edge cracking on bulk tungsten divertor components during 2017–2019 WEST operation *Nucl. Mater. Energy* **41** 101746
[51] Gallo A. *et al* 2024 Wall conditions in WEST during operations with a new ITER grade, actively cooled divertor *Nucl. Mater. Energy* **41** 101741
[52] Tu H., Wang S., Cui L., Cheng L., Lu G.-H., O'Connor D.J. and Shi L. 2021 The influence of impurities on the erosion of tungsten by low energy high flux deuterium plasma irradiation *J. Nucl. Mater.* **556** 153168
[53] Kenmotsu T., Ono T. and Wada M. 2011 Effect of deuterium retention upon sputtering yield of tungsten by deuterons *J. Nucl. Mater.* **415** S108–11
[54] Loarer T. *et al* 2020 Long discharges in a steady state with D_2 and N_2 on the actively cooled tungsten upper divertor in WEST *Nucl. Fusion* **60** 126046
[55] Balden M., Rohde V., Lindig S., Manhard A. and Krieger K. 2013 Blistering and re-deposition on tungsten exposed to ASDEX Upgrade divertor plasma *J. Nucl. Mater.* **438** S220–3